JGR Solid Earth

RESEARCH ARTICLE
10.1029/2022JB024530

Seismic Fault Slip Behavior Predicted From Internal Microphysical Processes

Jianye Chen[1], **Andre R. Niemeijer**[2], **and Christopher J. Spiers**[2]

[1]State Key Laboratory of Earthquake Dynamics, Institute of Geology, China Earthquake Administration, Beijing, China, [2]HPT Laboratory, Department of Earth Sciences, Utrecht University, Utrecht, The Netherlands

Key Points:

- A microphysical model is applied to simulate seismic fault slip in carbonate rocks
- Laboratory trends in fault mechanical behavior are captured
- Spatial and temporal evolution of microstructure and deformation mechanisms fit observations

Supporting Information:

Supporting Information may be found in the online version of this article.

Correspondence to:

J. Chen,
j.chen3@uu.nl

Citation:

Chen, J., Niemeijer, A. R., & Spiers, C. J. (2022). Seismic fault slip behavior predicted from internal microphysical processes. *Journal of Geophysical Research: Solid Earth*, *127*, e2022JB024530. https://doi.org/10.1029/2022JB024530

Received 6 APR 2022
Accepted 31 OCT 2022

Author Contributions:

Conceptualization: Jianye Chen, Andre R. Niemeijer, Christopher J. Spiers
Methodology: Jianye Chen
Supervision: Andre R. Niemeijer, Christopher J. Spiers
Validation: Jianye Chen, Andre R. Niemeijer
Writing – review & editing: Andre R. Niemeijer, Christopher J. Spiers

Abstract Earthquake simulation and hazard prediction are strongly hampered by insufficient physical knowledge of the constitutive behavior of faults. Laboratory studies of carbonate fault friction suggest that seismogenic rupture on faults in carbonate terrains can be explained by a transition from high friction at low initial sliding velocities (V) to low friction at seismic slip velocities, that is, by rapid dynamic weakening. One proposed explanation for this weakening, invokes frictional heating resulting in deformation by grain boundary sliding accommodated by solid-state diffusion (sometimes referred to as "viscous" or "superplastic" flow). We recently added this dynamic weakening mechanism to a microphysically based model addressing the (rate-and-state) frictional behavior of granular gouges undergoing low V shear characteristic of rupture nucleation and arrest. In the present study, we applied the full model to simulate seismic slip in laboratory carbonate faults. Assuming that slip localizes in a principal shear band within the fault (gouge) zone, and accounting for grain size evolution with velocity and temperature, the model reproduces the frictional, thermal and (micro-)structural evolution observed during seismic slip experiments. In particular, it predicts spatial and temporal evolutions of grain size, porosity, and dominant deformation mechanisms, within and outside the assumed shear band, consistent with trends identified in the laboratory and natural fault zones.

Plain Language Summary Improving the basis for earthquake hazard assessment relies in part on structural observation of natural fault zones, on laboratory experiments, and on theoretical developments. While quantitative models that reproduce the laboratory data on frictional slip on faults is the minimum necessary to simulate their mechanical behavior in nature, convincing models must ultimately also account for all key fault zone observations. Taking a fault in carbonate rock as an example, and using fundamental data on the microscale processes that lead to fault friction, this study takes a first step toward simulating the dynamic evolution and self-organization of internal fault zone (micro)structure, processes and properties during a seismic slip event. The results show that the model captures many key observations on seismic fault behavior, paving the way for still further improvements in developing a physics-based understanding of earthquake rupture in future.

1. Introduction

Following the highly destructive earthquakes in carbonate-dominated terrains such as the 2009 Mw 6.1 L'Aquila earthquake, and the 2008 Mw 7.9 Wenchuan earthquake, the frictional behavior of carbonate-hosted faults has attracted much attention, providing data for models of earthquake rupture nucleation and propagation in such terrains. The fault dynamics of carbonates are now recognized to include a spectrum of fault slip styles ranging from slow-slip events, slow earthquakes, and fast ruptures (Amorus et al., 2002; Chiaraluce, 2012; Crescentini et al., 1999; Valoroso et al., 2013). Experiments on carbonate friction have been accordingly performed under a wide range of slip velocities. At low sliding velocities characteristic of earthquake nucleation (~1 μm/s), carbonates show high, rate-and-state dependent friction (Scuderi et al., 2013; Verberne et al., 2015, 2014; Weeks, 1983; Weeks & Tullis, 1985) and fast healing (Carpenter et al., 2014; Chen et al., 2015), while at higher velocities rapid dynamic weakening occurs as expected during rupture propagation (v = ~1 m/s, Demurtas, Smith, Prior, Brenker, & Di Toro, 2019; De Paola et al., 2011, 2015; Green et al., 2015; Han et al., 2007; Ohl et al., 2020; Pozzi et al., 2018; Rempe et al., 2017; Siman-Tov et al., 2015, 2013; Smith et al., 2013, 2015; Spagnuolo et al., 2015; Tisato et al., 2012).

Building insights into the earthquake hazards should benefit from concerted efforts in structural observation of natural fault zones, laboratory experiments, and theoretical developments. Ideally, a theoretical model needs to

describe the friction behavior over the full velocity spectrum and essentially should incorporate key information of local conditions, for example, internal fault structure and in situ pressure, temperature and fluid conditions Aharonov & Scholz, 2018; Barbot, 2019; Beeler, 2009; Bizzarri, 2012; Harbord et al., 2021). While many aspects of the frictional behavior can be captured by the constitutive framework of rate-and-state friction or microphysically based models for the low velocities (e.g., Dieterich, 1979; Niemeijer & Spiers, 2007; Sleep, 1995), mechanistically based models addressing the full range of slip rates encountered in progressing from rupture nucleation to seismic slip are rare (Aharonov & Scholz, 2018). From the modeling perspective, this has been limited to combining the RSF descriptions at low velocities with flash heating/melting or thermal pressurization in the dynamic weakening range (Bizzarri, 2012; Noda et al., 2009; Noda & Lapusta, 2010; Thomas et al., 2014).

In a recent study (Chen et al., 2021), we have incorporated superplastic flow (i.e., grain boundary sliding with solid-state diffusion accommodation) activated by frictional heating into a microphysically based model (the "Chen-Niemeijer-Spiers" model, Chen & Spiers, 2016; Niemeijer & Spiers, 2007) that originally accounts for the (rate-and-state) frictional behavior of carbonate fault gouges at low velocities. The extended CNS model now covers the full spectrum of slip velocities from earthquake nucleation to seismic slip rates. The model results capture the main mechanical behavior seen in high-velocity friction experiments on room-dry calcite-rich rocks, including steady state and transient aspects, with a reasonable quantitative agreement but without the need to invoke thermal decomposition or pressurization effects. Beyond an agreement with the mechanical behavior, in this study, we aim to test our model against the microstructural observations of carbonate faults after seismic slip. To circumvent circular argumentation, we prescribe the initial microstructure of the fault zone (i.e., grain size and porosity), and the predicted evolution of microstructure and operating mechanisms will be compared with the observations and interpretations from experiments that were stopped at different shear displacements (Demurtas, Smith, Prior, Spagnuolo, & Di Toro, 2019; Pozzi et al., 2019, 2018; Smith et al., 2015). In all, we provide the first model that integrates different fault zone observations rather than using (empirical) friction parameters (i.e., rate-and-state dependent friction) and which predicts the frictional behavior, microstructural evolution, and dominant deformation mechanisms (DDMs).

2. Carbonate Slip Surface During Seismic Slip: Microstructure and Interpretation

Let us recap the microstructure evolution of a carbonate slip surface undergoing seismic slip, mainly based on laboratory high-velocity friction (HVF) studies that have systematically stopped experiments at different shear displacements. To avoid complexity, we will focus on the relatively short-displacement ones (<1 m) in which superplastic flow was generally interpreted to be the dominating weakening mechanism, at least during the nominal steady state (Demurtas, Smith, Prior, Spagnuolo, et al., 2019; Pozzi et al., 2019, 2018; Smith et al., 2015).

Typically, the evolution of shear strength in these experiments follows a characteristic weakening profile featured by four distinct phases (Figure 1a). Dynamic weakening is observed following a transient strengthening (*Stage I* and *II*); the lowered friction continues to decrease, reaching a nominal steady state, which is followed by a re-strengthening upon deceleration (*Stage III* and *IV*). Microstructural analyses of samples that have gone through the full given stages revealed the presence of a central layer of a few tens of micrometers in thickness (c., 25 μm), surrounded by well-sintered zones on both sides (SGZ, Figure 1b). This central layer, which is inferred to be the principal slip zone (PSZ), consists of a continuous layer of nano-calcite grains with a nominal grain size (d) of 10–700 nm in diameter, showing polygonal grain boundaries and high-angle junctions. Field studies of natural carbonate faults also found the existence of well-polished, glossy surfaces, usually termed "fault mirrors", consisting of tightly packed nanoparticles, with grain and grain boundary structures similar to those seen in the experiments (Fondriest et al., 2013; Ohl et al., 2020; Siman-Tov et al., 2013; Smith et al., 2013). As proposed by De Paola et al. (2015) and Green et al. (2015), the mechanism accommodating the high strain rate in the PSZ ($\dot{\gamma} > 10^3\ s^{-1}$, inset of Figure 1b) is most likely "superplastic flow", which forms the basis of our extended model.

As revealed by the experiments that stopped at different stages, the thickness, nominal grain size, and porosity of both the PSZ and the adjacent layers (e.g., SGZs) are continuously evolving (Demurtas, Smith, Prior, Spagnuolo, et al., 2019; Pozzi et al., 2019, 2018; Smith et al., 2015). At *Stage I*, the gouge layer is characterized by a brittle, cataclastic structure with the presence of Riedel and shear-parallel bands (Pozzi et al., 2018), and the PSZ starts to develop, with angular (sub)micron grains, high porosity, and relatively large thickness (~100 micron). From *Stage I to II*, the grains in the PSZ shown a remarkable reduction in size from (sub)micron to nanograins and the PSZ becomes increasingly more narrow as v approaches the seismic range (i.e., 0.1 m/s). By *Stage III*, the gouge

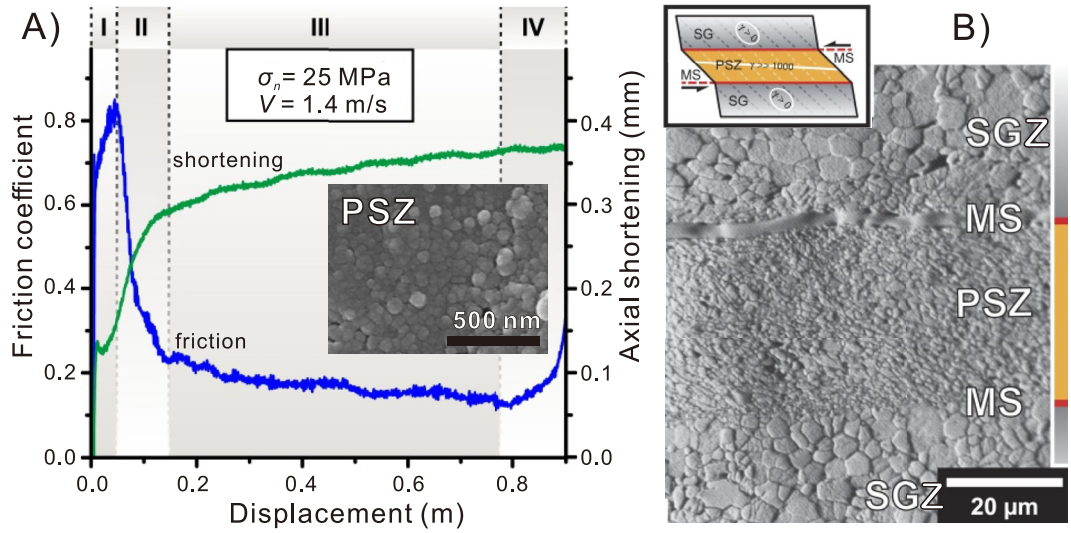

Figure 1. (a) Typical results from high-velocity friction (HVF) experiments on calcite gouge sheared at 1.4 m/s and 25 MPa normal stress with 0.9 m shear displacement (Pozzi et al., 2018). (b) A typical microstructure after 0.26 m displacement showing the principal slip zone (PSZ) and the surroundings sintering gradient zone (SGZ), as well as their interfaces which are interpreted as "mirror surfaces" (MS). The inset image in (a), which was derived from a sample sheared at 18 MPa normal stress (De Paola et al., 2015), shows that the PSZ consists of foam-textured nanocrystalline calcite, pointing to deformation by GBS with diffusional accommodation.

strength has reached a nominal steady state and the PSZ is characterized by low porosity and nearly uniform nanocrystalline grain size, with polygonal grain boundaries and high-angle junctions, suggesting a viscous flow process as described above. Occasionally, the grains in the PSZ after the experiments display weak elongation and minor oblique foliation (e.g., Pozzi et al., 2018), which was interpreted as the result of dynamic crystallization of nanoparticles and passive rotation of the grains. As demonstrated by Green et al. (2015), after the experiments, nanoparticles still survived on some patches of the slip surface, while the "pavement" structure covered a large portion as the result of the coalescence of growing nanocrystals, indicating that crystallization is most likely occurring during the annealing stage of the experiment (*Stage IV and after*). The PSZs after the experiment also show a crystallographic-preferred orientation and the presence of high dislocation density, indicating the operation of a dislocation-driven process (e.g., Pozzi et al., 2021; Smith et al., 2013). This is supported by a recent study of a natural carbonate slip surface, which reveals the coalescence of nanocrystalline (sub)grains featured by the high junction and small misorientation angles (Ohl et al., 2020). Individual subgrains typically possess high densities of dislocations, while locally, they are healed completely, showing a dislocation-free structure.

One interesting result of Pozzi et al. (2018) is that the mean grain size in the PSZ after 90 cm's slip is larger than that after 25 cm's slip at otherwise the same experimental conditions (700 vs. 300 nm); both are larger than the nominal grain size during steady state sliding (10–100 nm). On either side of the PSZ, the fault material (e.g., SGZ) may have experienced high temperatures and undergone crystal-plastic deformation, as manifested by microstructural evidence such as preferred grain elongation, a preferred crystallographic orientation, and grain growth (Demurtas, Smith, Prior, Spagnuolo, & Di Toro, 2019; Ohl et al., 2020; Siman-Tov et al., 2015; Smith et al., 2013), similar to the annealed portion on the slip surface. Characterized by nearly uniform grain size and low porosity, the SGZs show an increase in grain size and thickness with shear displacement (Demurtas, Smith, Prior, Spagnuolo, et al., 2019; Pozzi et al., 2019). The evolution of the microstructures during seismic slip suggests that there could have been transitions in DDM in both the PSZ and the adjacent layers (e.g., SGZ). The present study will test the microphysical model against the microstructural observations and interpretations summarized above.

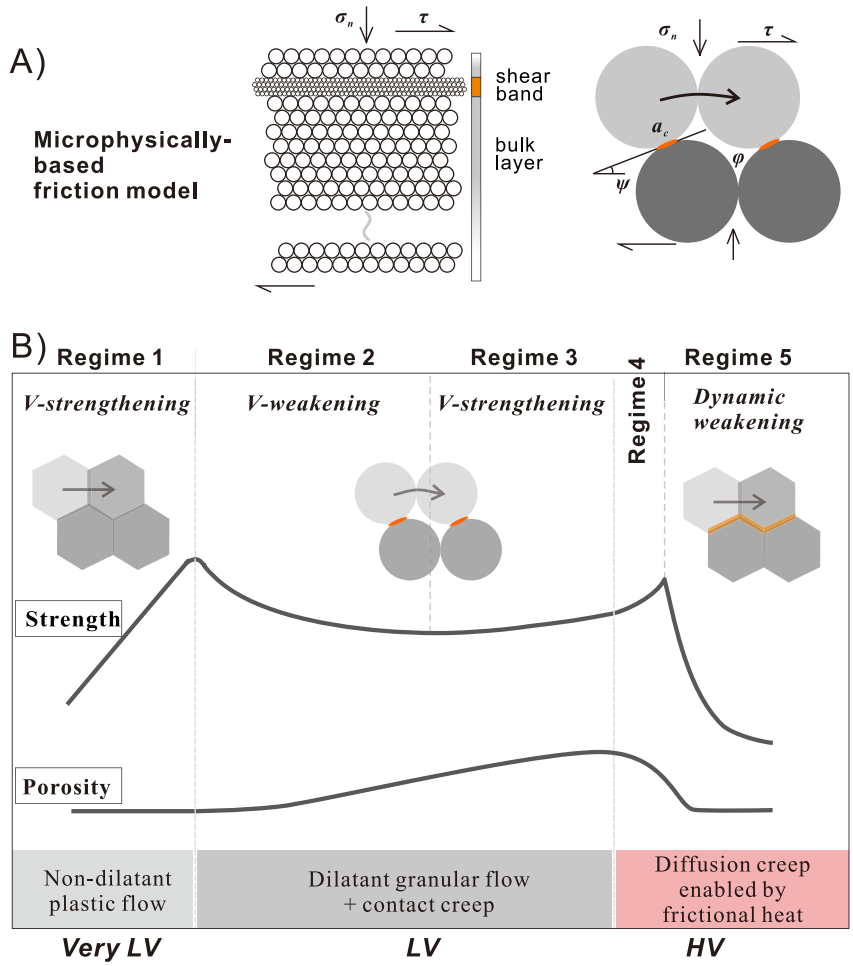

Figure 2. Schematic diagrams showing (a) the idealized microstructure and grain pack, and (b) the prediction of fault strength, slip zone porosity, and deformation regimes as a function of slip rate, as embodied in the CNS model (Chen et al., 2021). The typical microstructure shows slip localization into a shear band, where a four-grained unit cell is used to characterize the grain pack under active simple-shear deformation. As the slip rate increases, the unit strain deformation, as illustrated by the insets, undergoes a continuous transition in the dominant deformation mechanisms.

3. The CNS Model: From Earthquake Nucleation to Seismic Slip Rates

The CNS model considers the broad observation in both natural and laboratory fault zones that deformation tends to localize into a thin, finer-grained shear band developed within or at the boundary of the gouge layer (Figure 2a). The shear band and bulk gouge layer are composed of grains represented by spheres with the same packing pattern but with different mean diameters. Here we summarize the key relations or equations of the model.

1. In a 2-D geometry, the microstructure of the shear band is idealized using a four-grain unit cell. Porosity (φ), average dilatancy angle (ψ), and average contact area (a_c) form a set of three geometrically interrelated variables characterizing the microstructural state of the shear band. These are given by the approximate relations (Niemeijer & Spiers, 2007):

$$\tan\psi = 2H\left(\varphi_c - \varphi\right), \text{ and} \tag{1a}$$

$$a_c = 2\pi d^2\left(\varphi_c - \varphi\right)/z \tag{1b}$$

where φ_c is the critical-state porosity for granular flow, H is a constant related to the grain packing geometry, d is nominal grain diameter, and z is the average coordination number. The equation for the dilatancy angle (Equation 1a) is simply a functional form that roughly mimics the dependence of dilatancy angle on porosity

seen in experiments on granular materials such as sands and soils in the over-consolidated (sub-critical state porosity) regime (e.g., Bouckovalas et al., 2003). Both the shear band and the bulk layer are involved in the present model. In the following φ refers to the porosity in the shear band ($\varphi = \varphi^{sb}$), except when indicated otherwise.

2. The governing equations of the model were derived by applying a unified approach to a kinematic, energy-dissipating sliding system, that is, via the conservation of momentum and energy/entropy balance (or force balance) in a shearing gouge layer (Chen & Spiers, 2016; Niemeijer & Spiers, 2007). As given in detail by Chen and Spiers (2016), the constitutive equations governing the microstructural state and shear strength of the shear band are:

$$\frac{1}{(1-\varphi)}\frac{d\varphi}{dt} = \dot{\gamma}_{gr}\tan\psi - \dot{\varepsilon}_{pl} \tag{2a}$$

$$\mu \equiv \frac{\tau}{\sigma_n} = \frac{\tilde{\mu} + \tan\psi}{1 - \tilde{\mu}\tan\psi} \tag{2b}$$

In these equations, $\dot{\varepsilon}$ and $\dot{\gamma}$ indicate strain rates in the normal and shear directions, respectively. Subscript "*pl*" indicates strain rates due to a general "plastic" creep process, while "*gr*" indicates contributions by rate-independent granular flow. Grain boundary friction is assumed to be cohesion free and hence given by $\tilde{\mu} = \tilde{\tau}/\tilde{\sigma}_n$, where $\tilde{\sigma}_n$ and $\tilde{\tau}$ are the normal and shear stresses acting on sliding contacts, respectively. Based on analyses of the lattice scale frictional interactions on individual grain contacts involving both shear and normal components (Chen & Spiers, 2016), $\tilde{\mu}$ is expected to be intrinsically rate strengthening and can be reformulated in terms of the strain rate by granular flow ($\dot{\gamma}_{gr}$) as follows:

$$\tilde{\mu} = \tilde{\mu}^* + a_{\tilde{\mu}} ln\left(\dot{\gamma}_{gr}/\dot{\gamma}^*_{gr}\right). \tag{3}$$

Here $\tilde{\mu}^*$ is a reference $\tilde{\mu}$-value measured at a reference shear strain rate $\dot{\gamma}^*_{gr}$. The sensitivity parameter $a_{\tilde{\mu}}$ is given as $a_{\tilde{\mu}} = kT/\sigma_l\Omega$, where k the Boltzmann constant, T is temperature, Ω the activation volume, and σ_l the local normal stress supported by asperity contacts. This form of velocity-dependence of $\tilde{\mu}$ closely resembles the direct effect in the classical rate-and-state law (Nakatani, 2001; Rice, 2001). Notwithstanding this resemblance, the approach for deriving this relation is somewhat different, in that an atomic-scale jump process is considered to constitute the frictional slip at the nanometer scale of two grain contact asperities, rather than assuming deformation of an asperity through a dislocation glide or creep mechanism.

3. Incorporating the effect of porosity, the equations for a thermally activated creep mechanism are regularized as follows:

$$\dot{\gamma}_{pl}(\tau,\varphi,d,T) = A_t \exp\left(-\frac{E_a}{RT}\right)\frac{[\tau f_t(\varphi)]^n}{d^m}. \tag{4a}$$

$$\dot{\varepsilon}_{pl}(\varphi,d,T) = A_n \exp\left(-\frac{E_a}{RT}\right)\frac{[\sigma_n f_n(\varphi)]^n}{d^m}. \tag{4b}$$

which describe the shear and normal strain rates as a function of grain size (d), temperature (T), porosity (φ), and shear stresses (τ), assuming an isotropic creep process. Parameters A_t and A_n are pre-exponential geometrical factors in the shear and normal directions, respectively; E_a is the apparent activation energy, and n and m are the power exponents of stress and grain size, respectively. At a fixed porosity, the two geometrical factors are approximately related as $A_t \approx A_n/\tan\psi$. Other parameters (E_a, m, and n) follow the conventional creep laws and are assumed to be the same in both directions (Paterson & Olgaard, 2000). Without the porosity functions, $f_t(\varphi)$ and $f_n(\varphi)$, the above equations will reduce to the classical creep laws which are commonly derived from rheological experiments run at high temperature and pressure conditions, where the deforming material tends to have a low porosity. However, during a friction process, a granular gouge tends to be porous and can dilate to allow particles to roll, slide, and rearrange and thus accommodate displacement. Consequently, the local stresses transmitted across the grain contacts could be much higher than the macroscopic stresses (Figure 2b). Following our previous study (Chen et al., 2017), the porosity function in Equation 4a can be written as:

$$f_t(\varphi) = \left(1 - \frac{\varphi}{\varphi_c}\right)^{-p}. \tag{5a}$$

Here p is a sensitivity factor accounting for the contact area changes (hence contact stress magnitude) and the diffusion path length (if the grain boundary is involved), with porosity. To avoid negative porosity in the numerical computation, the porosity function in the normal direction is modified to

$$f_n(\varphi) = \left(\frac{\varphi_c - \varphi}{\varphi - \varphi_0}\right)^{-p}. \tag{5b}$$

In this formula, φ_0 is the limiting porosity (2%), below which compaction cannot occur (while shear creep still can, cf. Equation 5a, Chen et al., 2021). Note that the above creep equations (Equations 4 and 5) apply to both the shear band and the bulk layer.

4. Macroscopic shear rate of the sample deformation is rewritten as:

$$V = V_{gr} + V_{pl} = W_{sb}\dot{\gamma}_{gr} + \int_0^{W_{bulk}} \dot{\gamma}_{pl}\, dx. \tag{6}$$

Here W is the thickness and the subscripts "*sb*" and "*bulk*" represent the shear band and bulk layer, respectively. Granular flow is assumed to occur in the shear band, and multiple "plastic" creep processes can operate in the shear band and the bulk layer. $\dot{\gamma}_{gr}$ can be calculated by combining Equations 2b and 3, that is,

$$\dot{\gamma}_{gr} = \dot{\gamma}^*_{gr} \exp\left[\frac{\tau\,(1 - \tilde{\mu}^* \tan\psi) - \sigma_n\,(\tilde{\mu}^* + \tan\psi)}{a_{\tilde{\mu}}\,(\sigma_n + \tau \tan\psi)}\right]. \tag{7}$$

The creep processes are treated as operating in parallel, and the total shear strain rate is the summation of the individual process (i), they are,

$$\dot{\gamma}_{pl} = \sum \dot{\gamma}^i_{pl}(\tau, \varphi, d, T). \tag{8a}$$

Similarly, the rate of compaction, which enters. Equation 2a, can be written as

$$\dot{\varepsilon}_{pl} = \sum \dot{\varepsilon}^i_{pl}\,(\sigma_n, \varphi, d, T)\,. \tag{8b}$$

5. Massive nanocrystalline calcite is reported to be produced in both laboratory and natural faults after seismic slips (e.g., De Paola et al., 2015; Ohl et al., 2020). Based on the theoretical work of Sammis and Ben-Zion (2008) and Sleep (1995), we assumed the grain size to be strain rate dependent. Following our previous work (Chen et al., 2021), we applied the following empirical error function to allow d in the PSZ to decrease from d_0 to d_1 as V accelerates to ~0.1 m/s (or shear strain rate reaches ~5e3 s^{-1}, given a 20 μm thick PSZ):

$$d(V) = d_0 + (d_1 - d_0)\left[\frac{1}{2} + \frac{1}{2} erf\left(\frac{\log V - \log(0.1)}{\Delta}\right)\right]. \tag{9}$$

Adopting an error function, $erf(x) = \frac{2}{\sqrt{\pi}}\int_0^x \exp(-t^2)dt$, and using $\Delta = 0.25$, Equation 9 yields a smooth change in grain size from d_0 to d_1 over a 10-fold increase in velocity, that is, from 0.03 to 0.3 m/s, roughly consistent with the experimental observations (e.g., Smith et al., 2015).

Figure 2b shows a total of five steady state deformation regimes predicted by the CNS model as a function of velocity at constant (effective) normal stress and (ambient) temperature (Chen et al., 2021), based on the above model description and with frictional heating incorporated using a continuum framework. The transitions in deformation regime at the low velocities (*Regime* 1–2 and *Regime* 2–3) have been observed in many materials at varied temperature and pressure conditions such as calcite, quartz, halite, gypsum, serpentine, and natural and synthetic phyllosilicate-bearing gouges (Aharonov & Scholz, 2018; Chen et al., 2017). The transition in the high-velocity regimes (*Regime* 3–4 and *Regime* 4–5), which is presently limited to room temperature, have been observed in glass beads, serpentine, granite, calcite, and phyllosilicate-bearing gouges (e.g., Reches & Lockner, 2010; see a review in Bar-Sinai et al., 2014). Our model suggests that for carbonate rocks, the evolution of porosity is the key factor that bridges the transition in deformation mechanisms from *Regime* 4 to 5, namely, from granular flow involving (frictional) granular sliding to high-temperature GBS accommodated by diffusion creep (Ashby & Verrall, 1973; De Paola et al., 2015). Recently, the typical microstructure supporting GBS has been observed in other minerals or fault rocks under seismic slips (Pozzi et al., 2021). A final note is that

Figure 2b is a general prediction. Some regimes could be missing for different materials or the same material but at other ambient conditions (e.g., higher temperature). As demonstrated by Chen et al. (2021), the main mechanical trends seen in HVF experiments on room-dry carbonate rocks (*Stages I–IV*, Figure 1a) roughly correspond to the velocity and temperature dependence of steady state friction shown in Figure 2b, that is, the high-V regimes, *Regimes* 4–5.

3.1. Grain Growth Activated by Frictional Heating

As addressed earlier, microstructural observations showed evidence for grain growth in both the PSZ and the surrounding zones after the high-V friction experiments (Figures 1b, Demurtas, Smith, Prior, Brenker, et al., 2019; Green et al., 2015; Pozzi et al., 2019, 2018; Smith et al., 2013) or in natural seismic faults (Ohl et al., 2020; Smith et al., 2013). Using the well-known equation in a generalized Arrhenius form (e.g., Covey-Crump, 1997), the grain growth from the reduced size d_1 to a new size d can be described as:

$$d(t)^{\frac{1}{n}} - d_1^{\frac{1}{n}} = k \times \exp\left(\frac{-E_d}{RT}\right) \times t, \tag{10a}$$

where n is a dimensionless constant (not the stress exponent in the creep law), k is the pre-exponential rate constant, E_d is the apparent activation enthalpy of the process controlling the grain growth (note that E_d is different from the activity energy of a specific creep mechanism, cf. Equation 4), and t is the duration of the grain growth. As temperature (T) is evolving during an experiment, to use Covey-Crump's equation, we rewrite the equation into a differential form:

$$\frac{\partial d}{\partial t} = nkd^{\left(1-\frac{1}{n}\right)} exp\left(-\frac{E_d}{RT}\right). \tag{10b}$$

To avoid confusion, "∂" is used for differentiation while "d" for grain size.

The parameter values (n and k) given by Covey-Crump were obtained for calcite aggregates with porosity of less than 5% and might not be directly applicable to an actively shearing gouge, especially at the earlier stages where brittle, cataclastic deformation is dominating in the experiments. To explore this, we performed two control numerical simulations: the grains are allowed to grow only if the porosity is below a low level (5%) while there is no limit in the other case. The results showed that the predicted porosity evolution is essentially the same in the PSZ for both cases, while the porosity distribution in the bulk layer shows a minor difference. This seems intuitive since, as given by Equations 4 and 10, respectively, both the compaction rate and grain growth rate are tied to temperature following the Arrhenius law. At high porosities where Covey-Crump's equation may not apply, and granular flow dominates the deformation, the temperature is low, resulting in a low grain growth rate anyway. In other words, the grain growth rate only becomes significant at low porosity when the temperature becomes higher. Therefore, we applied the grain growth equation (Equation 10b) to the bulk gouge layer for simplicity. Gaining insight from the microstructure given by Green et al. (2015) (i.e., "pavement" structure and nanoparticle survivals), we expect that grains in the PSZ can not grow extensively on the slip surface while they are actively sliding, rolling, or neighbor swapping. For this reason, we assumed that grains in the PSZ start to grow from the deceleration stage.

3.2. Model Implementation

We will implement the above model into a continuum model of laboratory fault zones. A finite element model (FEM) is set up to calculate the temperature (T) evolution using the 1-D heat diffusion equation, $\rho c \frac{\partial T}{\partial t} = k \frac{\partial^2 T}{\partial x^2}$, where ρ is local gouge density, c is specific heat capacity, and k is thermal conductivity. We employed a one-dimensional (1-D), cross-fault model for simplicity, where x is the distance measured normal to the fault taking the center of the shear band (PSZ) as the origin (Figure 3c). Each component of the sample assembly used in the experiment (i.e., the gouge layer and adjacent loading blocks) has thermal properties shown in Table S1 in Supporting Information S1). To mimic the microstructure of a laboratory fault zone (Figure 2, Pozzi et al., 2018), the heat source is assumed to be localized at one of the boundaries of the gouge layer and was specified in terms of an internal boundary condition, $q = \tau V$ (i.e., assigned to one of the gouge-loading block interfaces, Figure 3c). Calculated temperatures from the FEM model were used to calculate the creep (Equation 4) and grain growth

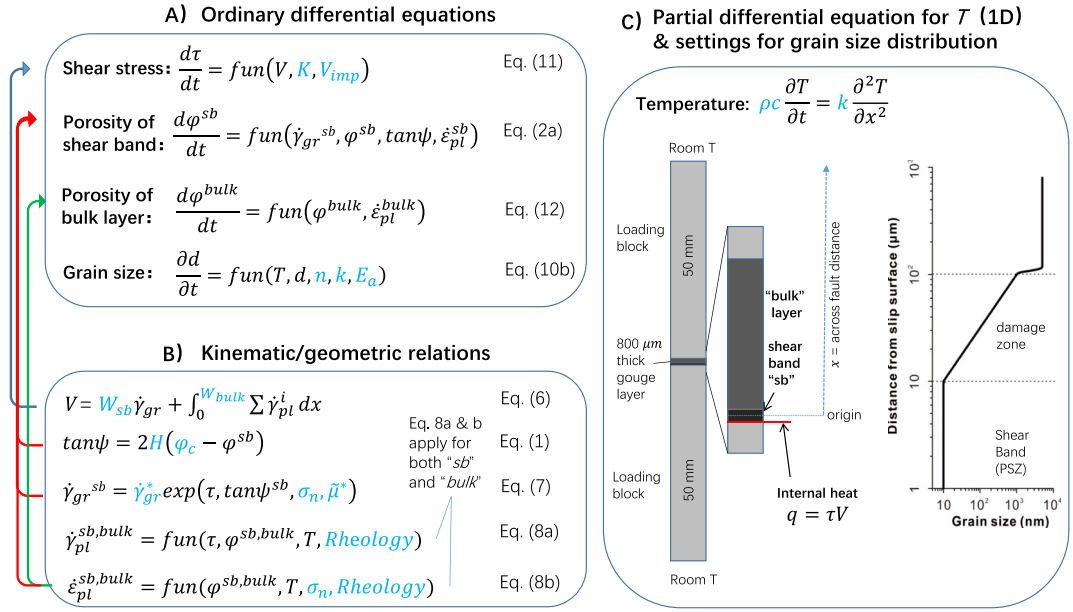

Figure 3. Coupled differential equations (a) and kinematic/geometric relations (b) used in the extended CNS model, plus (c) the finite element model (FEM) model configuration used to determine temperature (T) evolution normal to the principal slip zone (shear band) in a simulated high-velocity friction (HVF) experiment. The symbols shown in black are either independent variables (i.e., shear stress, porosity, grain size, and temperature) or functions thereof. Note that for some variables, here we insert the superscript "*sb*" and/or "*bulk*" to indicate where they apply (i.e., the shear band, bulk layer, or both), different from in the main text where they apply to the shear band in default except when indicated otherwise. Constants and material parameters are denoted in blue. *"Rheology"* refers to a collection of kinetic parameters characterizing the rheology associated with the assumed (inferred) deformation mechanism(s), such as those in Equation 4. Note that (c) illustrates the one-dimensional (1-D) FEM configuration and boundary conditions employed for simulating the 1-D temperature evolution in an experimental gouge layer and surrounding loading blocks. We assume that localized slip at the early stage of the simulated experiment produces a shear band and an adjacent damage/gouge zone characterized by a gradient in grain size distribution (see the text for detailed description).

rates (Equation 10). Since nearly uniform grain size and homogeneous deformation were observed in the PSZ (Figures 1b, Pozzi et al., 2018), we used the average temperature in the shear band to compute the average strain rates and grain growth rate (Chen et al., 2021).

The experimental fault is represented as a spring-slider system composed of a spring of stiffness K, activated by imposing a velocity at the load point (V_{imp}). Neglecting inertia, the shear stress evolution can be written in a time-derivative form as:

$$\frac{d\tau}{dt} = K(V_{imp} - V). \tag{11}$$

The final issue that remains is the compaction of the bulk layer. This does not affect stress evolution in the simulated fault zone. Since granular flow is assumed to be negligible in this layer, the governing equation for the bulk can accordingly be written as (cf. Equation 2a)

$$\frac{1}{(1-\varphi^{bulk})}\frac{d\varphi^{bulk}}{dt} = -\dot{\varepsilon}_{pl}^{bulk}. \tag{12}$$

Combination of the controlling equations for the evolution of shear stress (Equation 11), grain size (Equation 10b) and porosity (Equations 2a and 12), constitutes the governing ordinary differential equations (ODEs) of the present model. These ODEs, coupled with a 1-D FEM for temperature evolution, together with other relations, were solved simultaneously using the finite element package Comsol (see the couplings of differential equations and relations in Figure 3).

Table 1
Parameter Values Used for the Grain Size Evolution in Simulating the Lab Experiments

Para	Definition	Value or function	Source
Prescribed grain size reduction in the shear band: $d^{sb}(V) = d_0 + (d_1 - d_0)\left[\frac{1}{2} + \frac{1}{2}erf(\frac{\log V - \log(0.1)}{\Delta})\right]$			
d_0	Grain size during low-V slip	1 μm	$V < 0.06$ m/s
d_1	Minimum grain size during high-V slip	10–100 nm	$V > 0.18$ m/s
Δ	Factor for grain size reduction	0.25	
Grain size growth in the bulk layer, and in shear band during deceleration: $d^{\frac{1}{n}} - d_0^{\frac{1}{n}} = k \times \exp\left(\frac{-E_d}{RT}\right) \times t$			
k	Pre-exponential growth rate constant	3.55×10^{-2} $m^{1/n}s^{-1}$	Covey-Crump(1997)
n	A dimensionless constant	0.5	Covey-Crump(1997)
E_d	Activation enthalpy for grain growth	240 $kJmol^{-1}$	Covey-Crump(1997)
d	Pre-growth grain size in the PSZ[a]	10–100 nm	Microstructure
	Pre-growth grain size in the "damage" zone	With a (log-)linear gradient	Microstructure
	Truly initial grain size in the bulk layer	5–10 μm	Microstructure

[a]Since grains in the PSZ are not allowed to grow until the deceleration, the grain size will grow from the "initial" minimum grain size (d_1) after the prescribed reduction.

4. Numerical Simulation of Fault Behavior and Structural Evolution in HVF Experiments

In this section, using the early stage microstructure as the input to our model, we aim to produce the friction evolution and the (micro)structural evolution during typical HVF experiments. We mainly refer to the experimental work by Pozzi et al. (2019, 2018).

4.1. Model Settings and Parameters

We constructed a thermal structure based on the typical sample assembly used in the HVF experiments to simulate the temperature evolution. We assumed that the gouge layer of 800 μm in thickness is sandwiched between two 50 mm long host blocks made of Ti-alloy and further between a pair of 50 mm long loading columns made of stainless steel (e.g., Pozzi et al., 2018, Figure 3c). We assume an ambient temperature $T_0 = 20$°C and the densities and thermal properties of the different components are given in Table S1 in Supporting Information S1. To represent the typical microstructure of the gouge observed in the experiments (e.g., Figure 1), we considered a 20 μm thick PSZ developed at one margin of the gouge layer. Here we ignored the early cataclasis and localization processes that produce the shear band (or PSZ) and assumed a uniform grain size of 1 and 5 μm for the PSZ and the bulk layer, respectively. For both zones, we adopted an initial porosity of 18%. Following our previous study (Chen et al., 2021), the mean grain size in the PSZ was forced to decrease from 1 μm to 10 nm or 100 nm as V approaches ~0.1 m/s, following Equation 9. Note that such a prescribed change in grain size completes at a very short displacement (<5 mm). With continued sliding and temperature increase, the grains in both zones grow following Equation 10.

Parameter values for the grain growth were taken from Covey-Crump (1997) for fluid-absent conditions (Table 1). To allow static grain growth during cooling, our numerical simulations continued for another 10 s after terminating the slip. Following our previous study, we took the grain size-sensitive creep law to represent GBS accommodated by diffusion creep (Schmid et al., 1977), and the grain size-insensitive, dislocation creep law to represent the dislocation creep (Schmid et al., 1980; see parameter value in Table 1 of Chen et al., 2021). Other material parameters for a calcite fault gouge (H, $a_{\tilde{\mu}}$, $\tilde{\mu}^*$, φ_0, φ_c, and p) also follow the previous study (see Table S1 in Supporting Information S1). For all the simulations, we used a normal stress of 25 MPa. To be compatible with the initial microstructure assumed, we used an initial shear stress of 10 MPa (corresponding to a friction coefficient of 0.4) to ignore the early stage deformation processes. In this study, only stable behavior was simulated; therefore, a relatively stiff fault was assumed (300 MPa/mm).

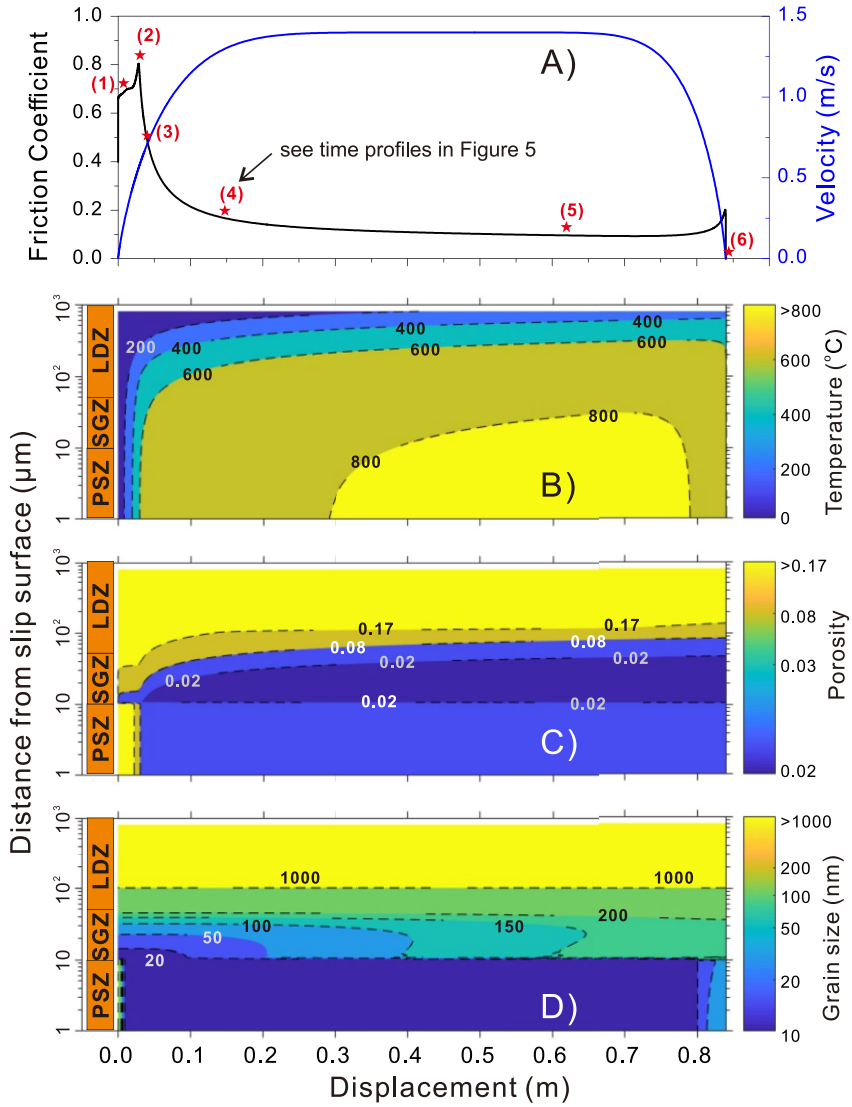

Figure 4. Reproducing the high-velocity friction (HVF) experiment by Pozzi et al. (2018). Predicted results for the evolution of (a), friction coefficient, and the spatial distribution of (b) temperature, (c) porosity, and (d) grain size over the gouge thickness, along with shear displacement. PSZ, principal slip zone (only half is presented); SGZ, sintering gradient zone; LDZ, less damage zone. Note that position in the gouge (thickness-vertical axis) is measured in terms of the log of distance from the center of the principal slip zone (PSZ), along with shear displacement. The grain size in (d) is color coded in the logarithmic scale, $\log(d)$, and porosity in (c) with respect to the two limit values and in the logarithmic scale, $\log((\varphi - \varphi_0) / (\varphi_c - \varphi))$.

4.2. Prediction of Friction Vs. Displacement Curve

The experiments were typically performed at pre-determined slip rates and displacements. The input V-profiles in our simulations mimicked those imposed in the experiments, including an acceleration, a period of constant-V sliding at 1.4 m/s, and deceleration, generating a total displacement (u_{max}) of 0.85 m. With the parameters given above, our model predicts the apparent friction coefficient curves with an initial value of 0.7 at short displacement, followed by a strong transient strengthening to a peak friction (μ_{pk}) of ~0.8, and then a sharp dynamic weakening to nominal steady state friction (μ_{nss}, Figure 4a). As slip continues at nearly constant V, μ_{nss} slightly decreases, followed by re-strengthening along with the deceleration. These results are generally consistent with the experimental results (cf. Figure 1a). The ability of the extended CNS model to reproduce experimental results has been demonstrated in our previous work (Chen et al., 2021) and includes reproduction of (a) steady state

friction as a function of slip rate (and temperature, cf. Figure 2b), and (b) transient friction as a function of displacement, both under varied experimental conditions of normal stress, maximum slip rate, and acceleration.

4.3. Predicted Spatial Distribution of T, φ, d: Evolution With Displacement

In the above simulations, we assumed a uniform initial grain size of 5 μm in the bulk layer. However, the microstructures of samples after short displacements ($u \leq 20$ mm) showed that a shear band never appear on its own but was (gradually) developed from a "damaged" zone, where the grain sizes increase as moving away from the shear band (Smith et al., 2013, 2015). To account for this observation, in our model, a 90 μm thick "damage" zone was set adjacent to the PSZ, where the initial grain sizes were assumed to have a log-linear gradient, that is, from 10 nm to 1 μm as moving away from the PSZ (Figure 3c). The remainder of the bulk layer was considered to be weakly affected by shear, with a uniform initial grain size of 5 μm.

For the assumed initial microstructure (i.e., in terms of grain size and porosity), the predicted friction curve as a function of shear displacement (u) is identical to the simulation reported above assuming a homogeneous bulk layer (Figure 4a). This is because the bulk layer contributes negligibly to the shear deformation. Since we have prescribed a reduction in grain size in the PSZ (from 1 μm to 10 nm), introducing a "damage" zone with no such evolution causes a sudden jump in the grain size distribution in the earliest stages of shearing. A more complex model, in which the grain size in the damage zone also evolves such that the grain size in the PSZ is always smaller, yielded identical results. Once again, this is because the damage zone contributes negligibly to the total shear deformation. In the present work, we, therefore, chose to use the simpler model without prescribing a grain size evolution in the damage zone. Figures 4b–4d further present the evolution of the spatial distributions of temperature, porosity, and grain size over the entire gouge layer thickness ($0 \leq x \leq 800$ μm), in the logarithmic scale. Defining $x = 0$ as the middle of the 20 μm thick PSZ, less than half of it (x = 1–10 μm) is presented and the adjacent layer includes a "damage" zone (x = 10–100 μm and the weakly deformed zone (x = 100–800 μm). The predicted temperature in the PSZ increases rapidly to ~600°C in a short displacement ($u \leq 3$ cm) after which temperature increases more slowly with the occurrence of dynamic weakening, reaching a maximum temperature of ~900°C just before deceleration (Figure 4b). The porosities in the PSZ remain at a high level at short displacement (>17% at $u \leq 3$ cm) and then collapse rapidly to a low value (~2.4%), slightly above the prescribed minimum ($\varphi_0 = 2\%$, Figure 4c). The fast changes in T and φ in the PSZ are associated with transient strengthening and dynamic weakening (cf. Figure 4a).

As temperature increases with displacement, the damage zone (x = 10–100 μm) also shows a reduction in porosity and a growth in grain size, especially in the vicinity of the PSZ where the temperature reaches high levels (>800°C, Figures 4c and 4d). As given by Equations 8 and 10, respectively, the rates of compaction and grain growth depend not only on temperature but also on the (concurrent) grain size. Recall that the initial grain sizes were set to increase log-linearly with distance to the PSZ in the damage zone. This gradient, together with T-dependent compaction and grain-growth rates, results in a special layer adjacent to the PSZ, characterized by close grain packing ($\varphi = \sim\varphi_0$) and nearly uniform grain size (10 μm $\leq x \leq$ 50 μm), which is consistent with the "sintering-gradient zone" (SGZ) defined by Pozzi et al. (2018). By contrast, in the remainder of the gouge layer (x = 50–800 μm), the porosity and grain sizes do not change much over the entire numerical experiment, which is hereafter referred to as the "less-damaged zone" (LDZ).

Figure 5 plots the across-fault profiles of porosity and grain size at different stages of the numerical experiments (refer to the stars in Figure 4a). The SGZ, characterized by low porosity and nearly uniform grain size, mainly develops during the dynamic weakening (from *Points* 2 to 5). Its thickness also increases with displacement, reaching ~40 μm by the end of the experiment (see the areas between the two vertical dashed lines). In the LDZ, the grain sizes barely change, but there is quite some compaction adjacent to the SGZ. The deformation map in the following section reveals that this is mainly caused by (grain size insensitive) dislocation creep as the temperature rises. To extract the overall features of different zones, the SGZ is defined as a portion of the bulk layer where the porosity has compacted to less than 3% (recall $\varphi_0 = 2\%$). The result shows that the SGZ starts to form with the onset of dynamic weakening ($u \sim 3$ cm) and grows to ~42 μm in thickness after the numerical experiment (Figure 6a). Interestingly, the (mean) porosities in the SGZ and PSZ cross over two times over the experiment (Figure 6b); namely, the SGZ has lower porosity than the PSZ except during the rapid dynamic weakening (3 cm $< u <$ 10 cm). Note that the initial porosities were assumed to be the same in both zones (18%). However, by imposing slip at the prescribed velocity, localized shearing in the PSZ will cause it to dilate and quickly reach

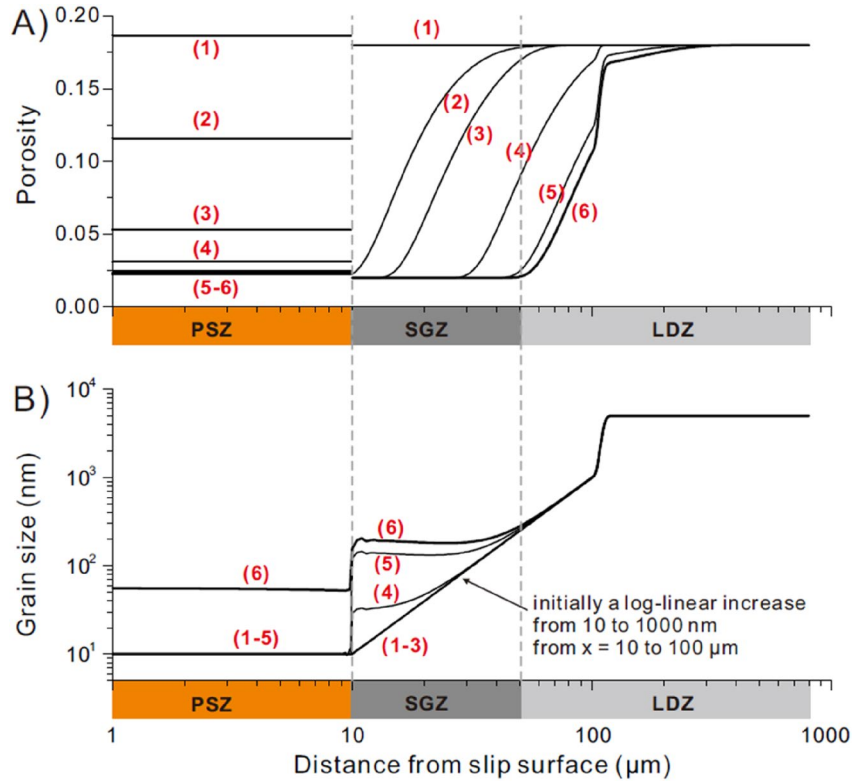

Figure 5. The predicted spatial distribution of (a) porosity and (b) grain size at a selection of shear displacements (see the stars in Figure 4a). Note that porosity and grain size continue to change after sliding stops (see the difference between Figures 5 and 6).

a quasi-static porosity of ~20% (close to the critical value, Figure 6b). By contrast, the non-shearing SGZ can only compact from 18% to lower porosity values, due to compaction creep enhanced by frictional heating. This, combined with much rapider compaction in the PSZ than in the SGZ due to the higher temperature (Figure 6), causes the first crossover. The second crossover, namely, to the slightly higher porosity in the PSZ than the SGZ at large displacement, is due to the operation of the dilatancy mechanism (i.e., granular flow) in the PSZ. As the SGZ widens, its mean grain size also increases from 40 to 200 nm, while in the PSZ, the grain size is only allowed to grow after deceleration, reaching 40 nm by the end of the numerical experiment (Figure 6c).

To explore the effects of the initial grain size and its distribution, we performed one simulation using 100 nm as the PSZ nominal grain size. In this case, grain sizes in the "damage zone" were set to increase log-linearly (from 100 nm to 4 μm), as the reference case, with the remainder of the bulk layer uniform at 10 μm. Using a larger minimum grain size, the friction peak is achieved at larger shear displacement (u = 45 vs. 28 mm in the d = 10 nm case). The peak is then followed by rapid slip weakening at similar weakening rates, finally reaching a slightly higher nominal steady state friction before the deceleration phase (μ_{nss} = 0.15 vs. 0.1, Figure 7a). The general features in the spatiotemporal evolution of temperature, porosity, and grain size are similar to the reference case (Figures 6d–7b). Specifically, with larger grain sizes, a higher temperature (T) is produced across the simulated gouge layer, with a maximum value of 1,210°C being reached in the PSZ before the deceleration phase (Figure 7b). The associated dynamic weakening occurs when T in the PSZ reaches ~800°C, which is higher than that in the 10 nm case (600°C). Using the same definition for SGZ ($\varphi \leq 3\%$), the thickness of SGZ grows to a maximum value of 43 μm (Figure S1 in Supporting Information S1). After the same shear displacement (u = 0.85 m), the final grain size in the PSZ increases from 100 nm to 1.8 μm, and that in the SGZ increases to ~6 μm (Figure 7c and Figure S1 in Supporting Information S1). The porosities in the PSZ and SGZ display much slower compaction compared to that in the 10 nm case (Figure 7c). Note that the PSZ has larger porosity than the adjacent SGZ, as in the 10 nm case (cf. Figure 4c). As explained earlier, this is due to the parallel operation of dilatant granular shear flow in the PSZ but not in the SGZ.

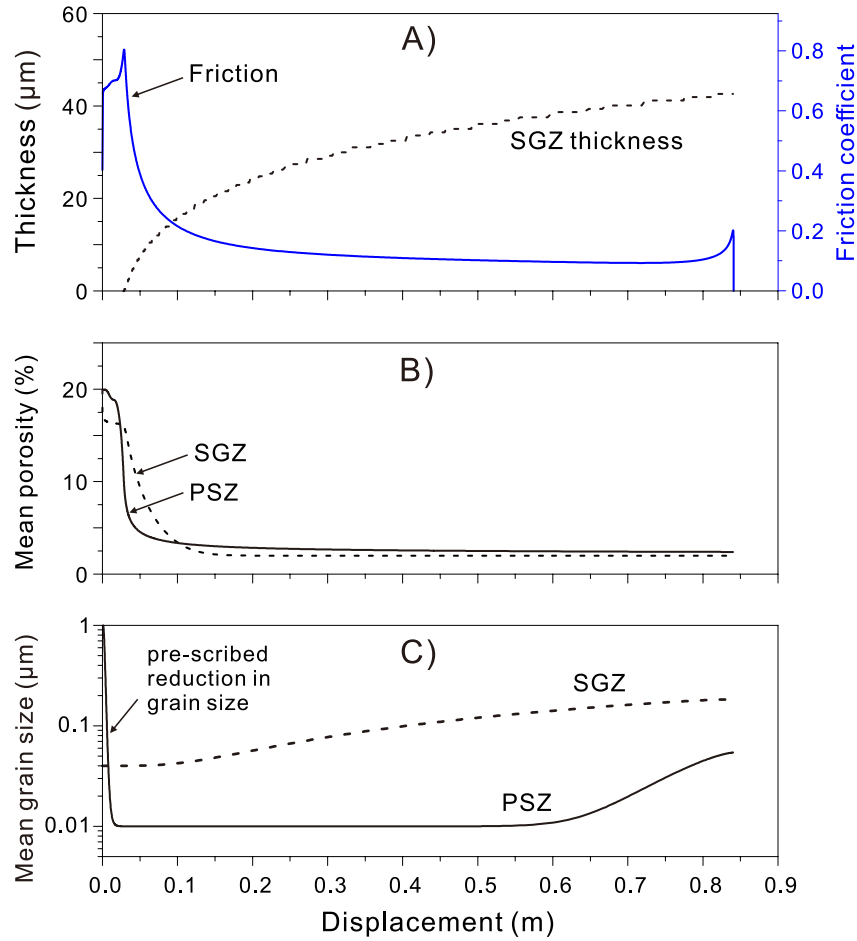

Figure 6. The predicted evolution of (a) friction, (b) the mean porosity, and (c) grain size in the principal slip zone (PSZ) and surrounding sintering gradient zone (SGZ), with shear displacement. The extracted SGZ thickness is also added in (a).

We further performed one simulation using 10 nm as the nominal grain size in the PSZ as the above reference case, but for the damage zone, we use a linear gradient, instead of a log-linear one, to represent the increase in grain size. The simulation results are given in Figures S2 and S3 in Supporting Information S1. Compared with the reference simulation, the results, including the evolution of friction, the porosity and grain size in the PSZ, are almost identical, except that a lightly narrower SGZ is produced (28 vs. 40 μm), with a slightly gentler compaction rate.

4.4. Predicted Spatial Distribution of Deformation Mechanisms: Evolution With Displacement

We next explored the spatial distribution of deformation mechanisms and how this varies in the simulated laboratory experiment. Since shear stress, porosity, temperature, and grain size are continuously evolving, the dominant (rate-controlling) deformation mechanism in the individual zones (i.e., PSZ, SGZ, and LDZ) may switch from one to another depending on their relative ease, that is, granular flow, dislocation creep, and GBS with accommodation by diffusion (or "diffusion creep" for expressing convenience).

We construct the DDMs for the 10 and 100 nm PSZ grain size cases. Figure 8 presents the evolution of friction coefficient and the contour maps for temperature and the DDM, using 100 nm as the PSZ grain size. As expected, most of the shear strain is accommodated by the PSZ (>99%). In this zone, there is a transition in the DDM from granular flow ($u \leq 3$ cm), via a short period of dislocation creep, to diffusion creep (Figure 8c). The deformation rate in the LDZ simply transitions from a negligible low level ($\dot{\gamma} \leq 1 \times 10^{-9}$ s^{-1}) to dislocation creep (e.g., $\dot{\gamma} \leq 0.07$ s^{-1} at $x = 200$ μm), however, due to the large grain size, its contribution to the total shear strain rate is still negligible (~0.0005%). Complex transitions in DDM are involved in the damage zone or the SGZ in particular.

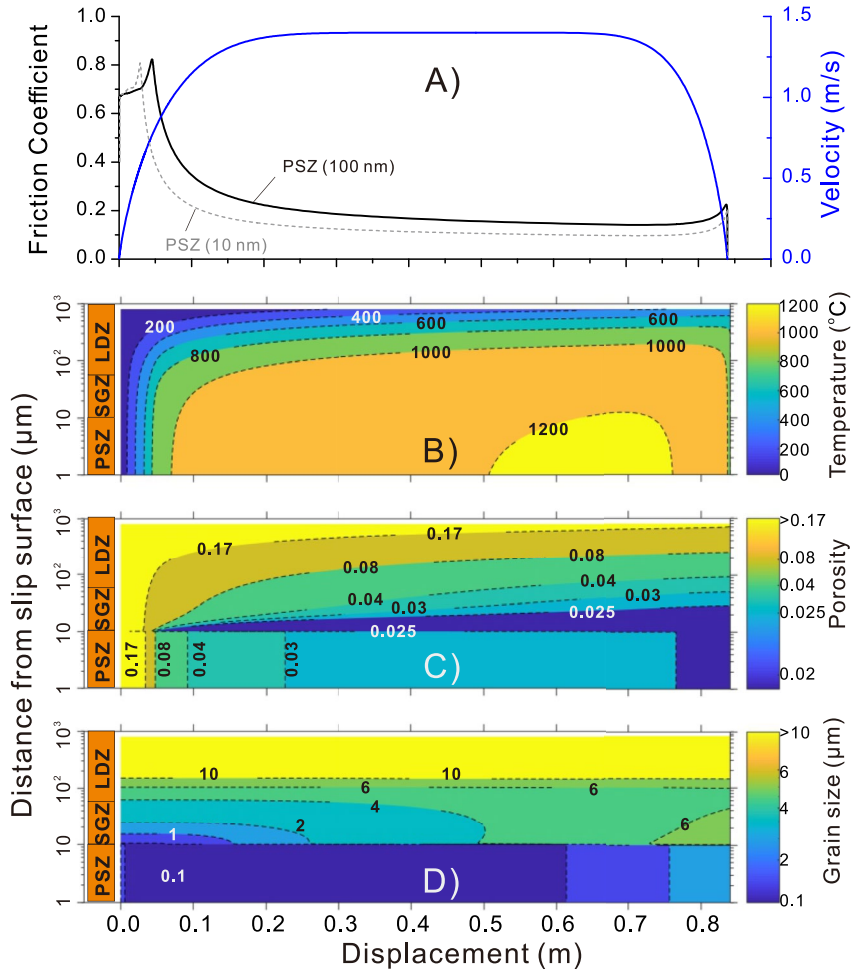

Figure 7. The evolution of (a) friction coefficient, as well as the spatial distribution of (b) temperature, (c) porosity, and (d) grain size over the logarithmic gouge thickness, along with shear displacement. Same simulation as shown in Figure 4 but using larger minimum grain sizes in the principal slip zone (PSZ) and the damage zone (100 nm). The friction curve from the reference case using 10 nm PSZ grain size is added for comparison (in dashed gray line).

The DDM switches from granular flow at a short distance ($u \leq 3$ cm), via dislocation creep (3 cm $\leq u \leq$ 10 cm), to diffusion creep (10 cm $\leq u \leq$ 60 cm, or during nominal steady state sliding), and back to dislocation creep as V decelerates (60 cm $\leq u \leq$ 85 cm). Therefore, in the SGZ, one could expect low porosity, uniform grain size, and features for dislocation creep after the experiment. Related microstructural evidence, such as preferred grain elongation and CPO, was indeed reported in the postmortem microstructures (e.g., Demurtas, Smith, Prior, Spagnuolo, et al., 2019; Pozzi et al., 2019; Smith et al., 2013). Although the strain rate by dislocation creep in the SGZ can be as high as 0.9 s^{-1} (evaluated at 5 μm away from the PSZ), it is only dominant during the deceleration phase (Figure 8c). Due to the limited shear strain accommodated by dislocation creep (<0.4), any CPO would not be very strong (Demurtas, Smith, Prior, Spagnuolo, et al., 2019).

We also constructed the DDM map for the 10 nm case (Figure S4 in Supporting Information S1). In general, smaller grain sizes cause shorter u_w, lower μ_{nss}, and lower temperatures; the deformation is more favorable for the diffusion-accommodated mechanisms. Except at the early stage where granular flow dominates, in the PSZ and SGZ, the deformation is dominated by grain boundary sliding with diffusion accommodation. In the LDZ, dislocation creep is the only deformation mechanism operating throughout the experiment, although the corresponding strain rates are extremely low (<10^{-8} s^{-1}).

To compare with the laboratory experiments that were stopped at different stages and revealed distinct microstructures, we next simulated a laboratory experiment with a shorter displacement (u_{max} = 0.27 m). Other settings

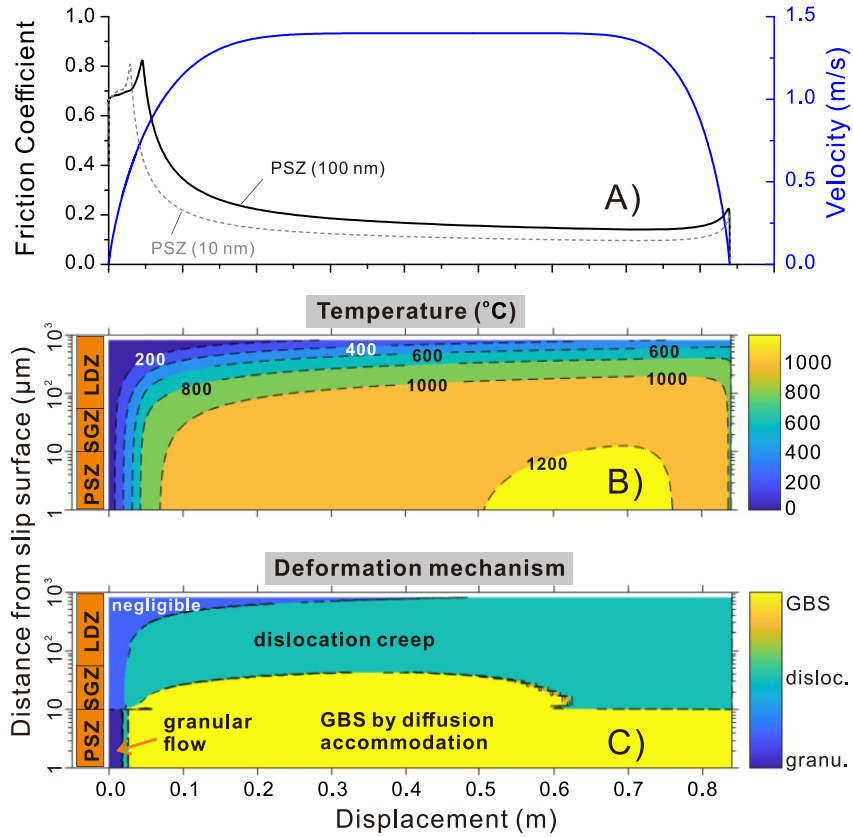

Figure 8. Constructed dominant deformation mechanism (DDM) map for a high-velocity friction (HVF) experiment. The evolution of (a) friction coefficient, as well as the spatial distribution of (b) temperature and (c) DDM over the logarithmic gouge thickness. All the results are derived from the simulation using 100 nm principal slip zone (PSZ) grain size. In (a), the friction curve from the reference case using 10 nm minimum PSZ grain size is added for comparison (in dashed gray line).

follow the case using a nominal grain size of 100 nm in the PSZ. As shown in Figure S5 in Supporting Information S1, the final grain sizes in the PSZ and SGZ are ~300 nm and 2 μm, respectively, which are smaller than those after 0.85 m of slip, where the final grain sizes are 1.8 and 6 μm, respectively. With a short displacement, the SGZ just started to develop after the experiment (4 μm in thickness), while after a long slip, the SGZ becomes 10 times wider (~40 μm). This growing feature in the PSZ and SGZ is consistent with the microstructures after the laboratory experiments (cf. Figure 3 of Pozzi et al., 2019). In terms of deformation mechanisms, with shorter displacement, granular flow contributes largely to the deformation during the deceleration stage, with shear strain rates up to 10 s^{-1} (Figure 9). This is because with a shorter displacement a more pronounced re-strengthening occurs (Figure 9a), which is favorable for the operation of granular flow (due to its higher stress sensitivity than a diffusion process), and also because the maximum temperature reached in the PSZ is lower so that as the temperature decreases during deceleration any diffusion process would easily lose its advantage. This prediction is again consistent with the observation that the PSZ sometimes loses its integrity after a laboratory experiment (see Figure 2 of Pozzi et al., 2018).

5. Capabilities and Limitations of the Extended CNS Model

5.1. Integration of Fault Zone Observations Using a Physics-Based Model

The microphysical model proposed in this study facilitates the integration of laboratory rheology data, fault structure, and geophysical observations to predict the frictional properties of a fault. Starting from the observations that similar (micro-)structures were observed in the PSZs representative of seismic slip, we extended an existing microphysically based friction model from low-velocities characteristic of earthquake nucleation to the high-V deformation regime by incorporating the DDM (superplastic flow) and grain growth recognized from

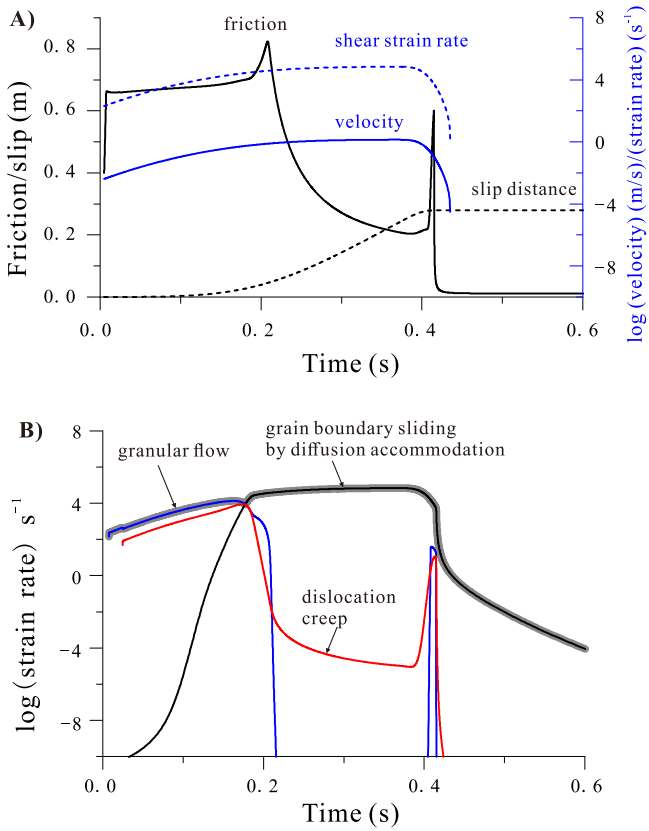

Figure 9. Numerical experiment with a short slip distance (0.27 m). (a) The time evolution of friction, slip distance, imposed velocity, and shear strain rate in the principal slip zone (PSZ). (b) Contribution of different (candidate) deformation mechanisms to shear strain rates in the PSZ. The thick gray line indicates the dominant mechanisms.

microstructural analyses (Chen et al., 2021). The model was then incorporated into the continuum framework of a spring-slider fault analog, simulating the evolution of shear stress, grain size, and porosity. The across-fault initial structure and thermal properties followed the laboratory or natural fault zones. The rheological parameters for the candidate deformation mechanisms and grain growth were obtained from independent (previous) laboratory work. The in situ normal pressures, ambient temperature, and far-field driven (boundary) conditions of the fault could be obtained from geological investigation and/or geophysical inversions. Incorporating these data, we have shown that the model results can nicely reproduce the transient frictional behavior observed in a typical HVF experiment. Remarkably, by the microphysically based nature, the model also predicts the evolution of fault (micro)structure (from a prescribed initial microstructure) and the crossovers of the DDMs across the fault zone (i.e., within and outside the PSZ), which are generally consistent with the interpretations from laboratory experiments that were stopped at different displacements (Figure 10). This is the first time that a friction model uses integrated observations from other fields than (empirical) friction parameters and predicts frictional behavior and the (self-choice) DDM by minimization of shear strain energy.

Technically, the model can be refined from experiments where most of the parameters are well known. The refined model can simulate the process on a natural fault plane filled with similar material. Practically, applying the model to nature requires a combination of the data mentioned above, including fault (micro)structure, rheological parameters of the candidate deformation mechanisms, and in situ *P*-*T*-fluid and loading conditions. Despite the uncertainties in some parameters, the model provides a physical basis that can bridge our knowledge and existing data from various aspects into a complete picture, with predictions for the microstructure that can be verified with observations from exhumed fault zones.

5.2. Limitation and Future Developments

Recently, Pozzi et al. (2021) have shown that superplastic (or viscous) flow might apply to a broad range of minerals other than calcite under room-dry conditions to accommodate the ultra-high strain rate during seismic slip (up to 10^5 s^{-1}) and therefore account for the dynamic weakening observed. Nonetheless, other dynamic mechanisms could also play a role in the dynamic weakening. First, the rate-dependent parameter of grain boundary friction $a_{\tilde{\mu}}$ depends on the contact stress and temperature. In the present work, we keep $a_{\tilde{\mu}}$ as a constant, however, during high-V sliding, the microscopic temperature on the asperities could be much higher than the macroscopic temperature due to processes such as flash heating (Harbord et al., 2021). Meanwhile, grain contacts will deform plastically and therefore change the local stresses. Aharonov and Scholz (2018) have considered the effects of temperature and local stress evolution on the direct rate-dependent parameter (a-value) in the framework of RSF theory. Their results showed incorporating these effects, together with the occurrence of flash melting, can cause a dramatic weakening of a quartz gouge. These factors need to be incorporated into the microphysical model. Another mechanism would be carbonate decomposition (Han et al., 2007). Although this reaction has an equivalent activation temperature (~600°C), due to the large mass loss in solid (~47%) it can exert a strong effect on reducing the effective pressure due to the released CO_2, which can even probably dominate the dynamic weakening, especially for the later stage of a seismic event.

It would be interesting to investigate the fault behavior at initially unstable conditions (e.g., at higher temperatures or lower stiffness), where carbonate fault gouges display V-weakening behavior so that fault instability and the runaway process can occur spontaneously. In Figure S6 in Supporting Information S1, we illustrate that a simulated laboratory fault can undergo a transition from stable to unstable (stick) slips as temperature increases due to frictional heating as higher normal stress (50 MPa) is applied. To further examine this, numerical simulations

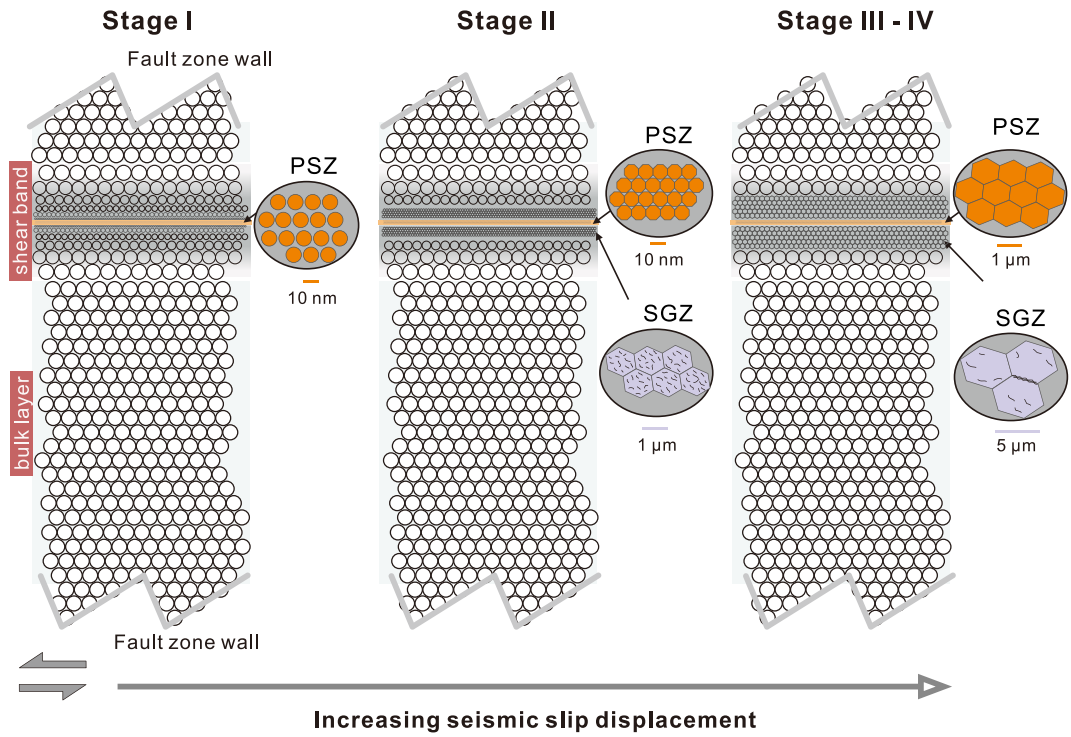

Figure 10. Internal microstructural evolution predicted by a microphysical model for seismic slip in a carbonate fault zone. The results agree well with the evolution of shear strength, microstructure, and dominant deformation mechanism seen in seismic slip experiments (PSZ, principal slip zone; SGZ, sintering gradient zone). Different stages (*Stage I–IV*) are defined by comparison with such experiments (e.g., Pozzi et al., 2018).

are planned in the future by implementing the present model into an earthquake cycle simulator (Lapusta & Rice, 2003; Noda et al., 2009; van den Ende et al., 2018). To produce cyclic fault behavior, we also need a rigorous governing equation for the grain size evolution (Barbot, 2019). Similar improvement is further needed for the evolution of (principal) slip zone thickness. Previous experiments suggested that dynamic weakening occurs in association with the spontaneous development of localized slip zones (Smith et al., 2015). Hypotheses of self-localization such as the competition between v-strengthening friction and a slip weakening mechanism need to be incorporated (Platt et al., 2014; Sleep et al., 2000). Finally, the present work only explored the HVF behavior of carbonate rocks under nominally dry conditions. One important effort would be to apply the model to other materials and fluid conditions (e.g., presence of pore water), accordingly incorporating other deformation mechanisms, such as pressure solution, as well as coupling pore fluid flow and pressure diffusion into the continuum model framework.

6. Conclusions

We have recently extended a microphysically based model (the "Chen-Niemeijer-Spiers") that originally accounts for the (rate-and-state) frictional behavior at low velocities, to high velocities where the operation of GBS with accommodation by solid-state diffusion within the PSZ, enabled by frictional heating, dominates the dynamic weakening. In this study, we applied the model that covers the full velocity spectrum to simulate seismic slip in the laboratory carbonate faults, focusing on the spatiotemporal evolution of fault (micro-)structure and deformation mechanisms.

Assuming that the grain size evolves with temperature following an Arrhenius dependence, we applied the model within the framework of a continuum model that represents typical high-V friction experiments. The model results capture the main trends of the mechanical data seen in the experiments; meanwhile, the model predicts an evolving spatial evolution of grain size, porosity, and DDMs, within and outside the shear band, which is consistent with the trends identified in the laboratory and in natural fault zones. In particular, the model predicts

a "sintering gradient zone" extending beyond the PSZ, characterized by low porosity and nearly uniform grain size. As velocity and hence temperature increase, the present model also predicts a continuous transition in DDM, from granular flow with partial accommodation by plasticity at low velocities and temperatures, to superplastic flow at high velocities and temperatures. Future work will consider implementing the extended model into earthquake cycle simulations.

Data Availability Statement

This is a theoretical work, and the codes and numerical data produced are all freely available online (https://doi.org/10.4121/20469435.v1).

Acknowledgments
This project is funded by the National Key R&D Program of China (2021YFC3000603), the European Research Council, grant SEISMIC (335915), and by the Netherlands Organisation for Scientific Research, VIDI grant (854.12.011), awarded to ARN.

References

Aharonov, E., & Scholz, C. H. (2018). A physics-based rock friction constitutive law: Steady state friction. *Journal of Geophysical Research*, *123*(2), 1591–1614. https://doi.org/10.1002/2016jb013829

Amoruso, A., Crescentini, L., Morelli, A., & Scarpa, R. (2002). Slow rupture of an aseismic fault in a seismogenic region of central Italy. *Geophysical Research Letters*, *29*(24), 721–724. https://doi.org/10.1029/2002gl016027

Ashby, M. F., & Verrall, R. A. (1973). Diffusion-accommodated flow and superplasticity. *Acta Metallurgica*, *21*(2), 149–163. https://doi.org/10.1016/0001-6160(73)90057-6

Barbot, S. (2019). Modulation of fault strength during the seismic cycle by grain size evolution around contact junctions. *Tectonophysics*, *765*, 129–145. https://doi.org/10.1016/j.tecto.2019.05.004

Bar-Sinai, Y., Spatschek, R., Brener, E. A., & Bouchbinder, E. (2014). On the velocity-strengthening behavior of dry friction. *Journal of Geophysical Research*, *119*(3), 1738–1748. https://doi.org/10.1002/2013JB010586

Beeler, N. M. (2009). Constructing constitutive relationships for seismic and aseismic fault Slip. *Pure and Applied Geophysics*, *166*(10–11), 1775–1798. https://doi.org/10.1007/s00024-009-0523-0

Bizzarri, A. (2012). Formulation of a fault governing law at high sliding speeds: Inferences from dynamic rupture models. *Earth and Planetary Science Letters*, *355–356*, 223–230. https://doi.org/10.1016/j.epsl.2012.09.007

Bouckovalas, G. D., Andrianopoulos, K. I., & Papadimitriou, A. G. (2003). A critical state interpretation for the cyclic liquefaction resistance of silty sands. *Soil Dynamics and Earthquake Engineering*, *23*(2), 115–125. https://doi.org/10.1016/s0267-7261(02)00156-2

Carpenter, B. M., Scuderi, M. M., Collettini, C., & Marone, C. (2014). Frictional heterogeneities on carbonate-bearing normal faults: Insights from the Monte Maggio Fault, Italy. *Journal of Geophysical Research*, *119*(12), 9062–9076. https://doi.org/10.1002/2014jb011337

Chen, J., Niemeijer, A. R., & Spiers, C. J. (2017). Microphysically derived expressions for rate-and-state friction parameters, a, b, and D_c. *Journal of Geophysical Research*, *122*(12), 9627–9657. https://doi.org/10.1002/2017jb014226

Chen, J., Niemeijer, A. R., & Spiers, C. J. (2021). Microphysical modeling of carbonate fault friction at slip rates spanning the full seismic cycle. *Journal of Geophysical Research*, *126*(3), e2020JB021024. https://doi.org/10.1029/2020jb021024

Chen, J., & Spiers, C. J. (2016). Rate and state frictional and healing behavior of carbonate fault gouge explained using microphysical model. *Journal of Geophysical Research*, *121*(12), 8642–8665. https://doi.org/10.1002/2016jb013470

Chen, J., Verberne, B. A., & Spiers, C. J. (2015). Effects of healing on the seismogenic potential of carbonate fault rocks: Experiments on samples from the Longmenshan Fault, Sichuan, China. *Journal of Geophysical Research*, *120*(8), 5479–5506. https://doi.org/10.1002/2015jb012051

Chiaraluce, L. (2012). Unravelling the complexity of Apenninic extensional fault systems: A review of the 2009 L'Aquila earthquake (Central Apennines, Italy). *Journal of Structural Geology*, *42*, 2–18. https://doi.org/10.1016/j.jsg.2012.06.007

Covey-Crump, S. J. (1997). The normal grain growth behavior of nominally pure calcitic aggregates. *Contributions to Mineralogy and Petrology*, *129*(2–3), 239–254. https://doi.org/10.1007/s004100050335

Crescentini, L., Amoruso, A., & Scarpa, R. (1999). Constraints on slow earthquake dynamics from a swarm in central Italy. *Science*, *286*(5447), 2132–2134. https://doi.org/10.1126/science.286.5447.2132

Demurtas, M., Smith, S. A. F., Prior, D. J., Brenker, F. E., & Di Toro, G. (2019). Grain size sensitive creep during simulated seismic slip in nanogranular fault gouges: Constraints from transmission Kikuchi diffraction (TKD). *Journal of Geophysical Research*, *124*(10), 10197–10209. https://doi.org/10.1029/2019jb018071

Demurtas, M., Smith, S. A. F., Prior, D. J., Spagnuolo, E., & Di Toro, G. (2019). Development of crystallographic preferred orientation during cataclasis in low-temperature carbonate fault gouge. *Journal of Structural Geology*, *126*, 37–50. https://doi.org/10.1016/j.jsg.2019.04.015

de Paola, N., Hirose, T., Mitchell, T., Di Toro, G., Togo, T., & Shimamoto, T. (2011). Fault lubrication and earthquake propagation in thermally unstable rocks. *Geology*, *39*(1), 35–38. https://doi.org/10.1130/g31398.1

De Paola, N., Holdsworth, R. E., Viti, C., Collettini, C., & Bullock, R. (2015). Can grain size sensitive flow lubricate faults during the initial stages of earthquake propagation? *Earth and Planetary Science Letters*, *431*, 48–58. https://doi.org/10.1016/j.epsl.2015.09.002

Dieterich, J. H. (1979). Modeling of rock friction: 1. Experimental results and constitutive equations. *Journal of Geophysical Research*, *84*(B5), 2161. https://doi.org/10.1029/JB084iB05p02161

Fondriest, M., Smith, S. A. F., Candela, T., Nielsen, S. B., Mair, K., & Di Toro, G. (2013). Mirror-like faults and power dissipation during earthquakes. *Geology*, *41*(11), 1175–1178. https://doi.org/10.1130/g34641.1

Green, H. W., Shi, F., Bozhilov, K., Xia, G., & Reches, Z. (2015). Phase transformation and nanometric flow cause extreme weakening during fault slip. *Nature Geoscience*, *8*(6), 484–489. https://doi.org/10.1038/ngeo2436

Han, R., Shimamoto, T., Hirose, T., Ree, J.-H., & Ando, J. I. (2007). Ultralow friction of carbonate faults caused by thermal decomposition. *Science*, *316*(5826), 878–881. https://doi.org/10.1126/science.1139763

Harbord, C., Brantut, N., Spagnuolo, E., & Di Toro, G. (2021). Fault friction during simulated seismic slip pulses. *Journal of Geophysical Research*, *126*(8), e2021JB022149. https://doi.org/10.1029/2021jb022149

Lapusta, N., & Rice, J. R. (2003). Nucleation and early seismic propagation of small and large events in a crustal earthquake model. *Journal of Geophysical Research*, *108*(B4), 1–18. https://doi.org/10.1029/2001jb000793

Nakatani, M. (2001). Conceptual and physical clarification of rate and state friction: Frictional sliding as a thermally activated rheology. *Journal of Geophysical Research*, *106*(B7), 13347–13380. https://doi.org/10.1029/2000jb900453

Niemeijer, A. R., & Spiers, C. J. (2007). A microphysical model for strong velocity weakening in phyllosilicate-bearing fault gouges. *Journal of Geophysical Research*, *112*(B10), B10405. https://doi.org/10.1029/2007jb005008

Noda, H., Dunham, E. M., & Rice, J. R. (2009). Earthquake ruptures with thermal weakening and the operation of major faults at low overall stress levels. *Journal of Geophysical Research*, *114*(B7), B07302. https://doi.org/10.1029/2008JB006143

Noda, H., & Lapusta, N. (2010). Three-dimensional earthquake sequence simulations with evolving temperature and pore pressure due to shear heating: Effect of heterogeneous hydraulic diffusivity. *Journal of Geophysical Research*, *115*(B12), B12314. https://doi.org/10.1029/2010JB007780

Ohl, M., Plümper, O., Chatzaras, V., Wallis, D., Vollmer, C., & Drury, M. (2020). Mechanisms of fault mirror formation and fault healing in carbonate rocks. *Earth and Planetary Science Letters*, *530*, 115886. https://doi.org/10.1016/j.epsl.2019.115886

Paterson, M. S., & Olgaard, D. L. (2000). Rock deformation tests to large shear strains in torsion. *Journal of Structural Geology*, *22*(9), 1341–1358. https://doi.org/10.1016/s0191-8141(00)00042-0

Platt, J. D., Rudnicki, J. W., & Rice, J. R. (2014). Stability and localization of rapid shear in fluid-saturated fault gouge: 2. Localized zone width and strength evolution. *Journal of Geophysical Research: Solid Earth*, *119*(5), 4334–4359. https://doi.org/10.1002/2013JB010711

Pozzi, G., De Paola, N., Holdsworth, R. E., Bowen, L., Nielsen, S. B., & Dempsey, E. D. (2019). Coseismic ultramylonites: An investigation of nanoscale viscous flow and fault weakening during seismic slip. *Earth and Planetary Science Letters*, *516*, 164–175. https://doi.org/10.1016/j.epsl.2019.03.042

Pozzi, G., De Paola, N., Nielsen, S. B., Holdsworth, R. E., & Bowen, L. (2018). A new interpretation for the nature and significance of mirror-like surfaces in experimental carbonate-hosted seismic faults. *Geology*, *46*(7), 583–586. https://doi.org/10.1130/g40197.1

Pozzi, G., De Paola, N., Nielsen, S. B., Holdsworth, R. E., Tesei, T., Thieme, M., & Demouchy, S. (2021). Coseismic fault lubrication by viscous deformation. *Nature Geoscience*, *16*(4), 437–442. https://doi.org/10.1038/s41561-021-00747-8

Reches, Z. E., & Lockner, D. A. (2010). Fault weakening and earthquake instability by powder lubrication. *Nature*, *467*(7314), 452–455. https://doi.org/10.1038/nature09348

Rempe, M., Smith, S., Mitchell, T., Hirose, T., & Di Toro, G. (2017). The effect of water on strain localization in calcite fault gouge sheared at seismic slip rates. *Journal of Structural Geology*, *97*, 104–117. https://doi.org/10.1016/j.jsg.2017.02.007

Rice, J. R., Lapusta, N., & Ranjith, K. (2001). Rate and state dependent friction and the stability of sliding between elastically deformable solids. *Journal of the Mechanics and Physics of Solids*, *49*(9), 1865–1898. https://doi.org/10.1016/S0022-5096(01)00042-4

Sammis, C. G., & Ben-Zion, Y. (2008). Mechanics of grain size reduction in fault zones. *Journal of Geophysical Research*, *113*(B2), B02306. https://doi.org/10.1029/2006JB004892

Schmid, S. M., Boland, J. N., & Paterson, M. S. (1977). Superplastic flow in fine-grained limestone. *Tectonophysics*, *43*(3–4), 257–291. https://doi.org/10.1016/0040-1951(77)90120-2

Schmid, S. M., Paterson, M. S., & Boland, J. N. (1980). High-temperature flow and dynamic recrystallization in Carrara Marble. *Tectonophysics*, *65*(3–4), 245–280. https://doi.org/10.1016/0040-1951(80)90077-3

Scuderi, M. M., Niemeijer, A. R., Collettini, C., & Marone, C. (2013). Frictional properties and slip stability of active faults within carbonate-evaporite sequences: The role of dolomite and anhydrite. *Earth and Planetary Science Letters*, *369*, 220–232. https://doi.org/10.1016/j.epsl.2013.03.024

Siman-Tov, S., Aharonov, E., Boneh, Y., & Reches, Z. (2015). Fault mirrors along carbonate faults: Formation and destruction during shear experiments. *Earth and Planetary Science Letters*, *430*, 367–376. https://doi.org/10.1016/j.epsl.2015.08.031

Siman-Tov, S., Aharonov, E., Sagy, A., & Emmanuel, S. (2013). Nanograins form carbonate fault mirrors. *Geology*, *41*(6), 703–706. https://doi.org/10.1130/g34087.1

Sleep, N. H. (1995). Ductile creep, compaction, and rate and state dependent friction within major fault zones. *Journal of Geophysical Research*, *100*(B7), 13065–13080. https://doi.org/10.1029/94jb03340

Sleep, N. H., Richardson, E., & Marone, C. (2000). Physics of strain localization in synthetic fault gouge. *Journal of Geophysical Research*, *105*(B11), 25875–25890. https://doi.org/10.1029/2000jb900288

Smith, S. A. F., Di Toro, G., Kim, S., Ree, J.-H., Nielsen, S., Billi, A., & Spiess, R. (2013). Coseismic recrystallization during shallow earthquake slip. *Geology*, *41*(1), 63–66. https://doi.org/10.1130/g33588.1

Smith, S. A. F., Nielsen, S., & Di Toro, G. (2015). Strain localization and the onset of dynamic weakening in calcite fault gouge. *Earth and Planetary Science Letters*, *413*, 25–36. https://doi.org/10.1016/j.epsl.2014.12.043

Spagnuolo, E., Plümper, O., Violay, M., Cavallo, A., & Di Toro, G. (2015). Fast-moving dislocations trigger flash weakening in carbonate-bearing faults during earthquakes. *Scientific Reports*, *5*(1), 16112. https://doi.org/10.1038/srep16112

Thomas, M. Y., Lapusta, N., Noda, H., & Avouac, J.-P., (2014). Quasi-dynamic versus fully dynamic simulations of earthquakes and aseismic slip with and without enhanced coseismic weakening. *Journal of Geophysical Research*, *119*(3), 1986–2004. https://doi.org/10.1002/2013JB010615

Tisato, N., Di Toro, G., De Rossi, N., Quaresimin, M., & Candela, T. (2012). Experimental investigation of flash weakening in limestone. *Journal of Structural Geology*, *38*, 183–199. https://doi.org/10.1016/j.jsg.2011.11.017

Valoroso, L., Chiaraluce, L., Piccinini, D., Di Stefano, R., Schaff, D., & Waldhauser, F. (2013). Radiography of a normal fault system by 64,000 high-precision earthquake locations: The 2009 L'Aquila (central Italy) case study. *Journal of Geophysical Research*, *118*(3), 1156–1176. https://doi.org/10.1002/jgrb.50130

Van den Ende, M. P. A., Chen, J., Ampuero, J.-P., & Niemeijer, A. R. (2018). A direct comparison between rate-and-state friction and microphysical models, based on earthquake cycle simulations. *Tectonophysics*, *733*, 273–295. https://doi.org/10.1016/j.tecto.2017.11.040

Verberne, B. A., Niemeijer, A. R., De Bresser, J. H. P., & Spiers, C. J. (2015). Mechanical behavior and microstructure of simulated calcite fault gouge sheared at 20°C–600°C: Implications for natural faults in limestones. *Journal of Geophysical Research*, *120*(12), 8169–8196. https://doi.org/10.1002/2015JB012292

Verberne, B. A., Spiers, C. J., Niemeijer, A. R., Bresser, J. H. P., De Winter, D. A. M., & Plümper, O. (2014). Frictional properties and microstructure of calcite-rich fault gouges sheared at sub-seismic sliding velocities. *Pure and Applied Geophysics*, *171*(10), 2617–2640. https://doi.org/10.1007/s00024-013-0760-0

Weeks, J. D. (1983). Constitutive laws for high-velocity frictional sliding and their influence on stress drop during unstable slip. *Journal of Geophysical Research*, *17*(B10), 637–648. https://doi.org/10.1029/93jb00356

Weeks, J. D., & Tullis, T. E. (1985). Frictional sliding of dolomite: A variation in constitutive behavior. *Journal of Geophysical Research*, *90*(B9), 7821–7826. https://doi.org/10.1029/jb090ib09p07821